



INSTITUT DE FRANCE
Académie des sciences

Comptes Rendus

Chimie


Qichao Wu, Rongli Jiang, Huaiwen Liu, Xiaojiang Li and Dan Xie

Facile synthesis of core-shell porous Fe₃O₄@carbon microspheres with high lithium storage performance

Volume 23, issue 4-5 (2020), p. 279-289.

<<https://doi.org/10.5802/crchim.18>>

© Académie des sciences, Paris and the authors, 2020.
Some rights reserved.

 This article is licensed under the
CREATIVE COMMONS ATTRIBUTION 4.0 INTERNATIONAL LICENSE.
<http://creativecommons.org/licenses/by/4.0/>



*Les Comptes Rendus. Chimie sont membres du
Centre Mersenne pour l'édition scientifique ouverte*
www.centre-mersenne.org



Full paper / *Mémoire*

Facile synthesis of core–shell porous Fe₃O₄@carbon microspheres with high lithium storage performance

Qichao Wu^a, Rongli Jiang^{*, a}, Huaiwen Liu^a, Xiaojiang Li^a and Dan Xie^a

^a College of Chemical Engineering and Technology, China University of Mining and Technology, No. 1, Daxue Road, Xuzhou City 221116, Jiangsu Province, China

E-mails: wqcchemistry16@163.com (Q. Wu), ronglij@cumt.edu.cn (R. Jiang), liuhuaiwen.cn@gmail.com (H. Liu), lxjchemistry19@163.com (X. Li), xdchemistry19@163.com (D. Xie)

Abstract. Core–shell porous Fe₃O₄@C (CP-Fe₃O₄@C) microspheres were synthesized using an environmentally viable hydrothermal method. Carbonization can reduce Fe₂O₃ and provide a conductive coating simultaneously. CP-Fe₃O₄@C microspheres as an active material for Lithium-ion batteries demonstrate pseudocapacity for improved rate performance. With a distinct nanostructure and pseudocapacitive effect, the CP-Fe₃O₄@C microspheres show excellent electrochemical performance (~785 mAh·g⁻¹ at 0.3 A·g⁻¹ after 200 cycles). Capacity measurements of CP-Fe₃O₄@C microspheres suggest near 90% pseudocapacitance at relatively low scan rates (5 mV·s⁻¹).

Keywords. Lithium-ion batteries, Fe₃O₄, Porous core–shell structures, Carbon.

Manuscript received 18th December 2019, revised 12th February 2020, accepted 14th February 2020.

1. Introduction

Microelectronic technology continues to advance in the 21st century, with an increase in the number of microelectronic devices and a higher consumer demand for power sources. Lithium-ion batteries (LIBs) have clear and obvious advantages and continue to dominate the market [1–4]. Transition metal oxides were considered for LIB anode materials in early 2000 due to their high capacities stemming from conversion reaction mechanisms [5–7]. Fe₃O₄ was among these early studied anode materials with a high capacity (theoretical value 926 mAh·g⁻¹) [8–10]. However, during cycling, Fe₃O₄

expands and breaks, causing rapid loss of capacity. Additionally, the conductivity of Fe₃O₄ is poor [11]. Carbon coating was found to help alleviate these problems, both addressing Fe₃O₄ volume expansion during cycling and preventing particle agglomeration [12–14]. More importantly, the carbon layer not only improved the conductivity of the electrode but also stabilized the solid electrolyte interface (SEI), which greatly improved the cycle life and rate capability of LIBs [15–17]. Further research in materials design pushed for Fe₃O₄ with a porous or hollow structure, which improves electrode reversibility and active material/electrolyte contact [18–20]. Recently, Wang *et al.* reported a novel Fe₃O₄@Carbon yolk–shell nanorod anode material by a one-pot method. The voids in the Fe₃O₄@Carbon core–shell nanorods were beneficial for volume expansion and

* Corresponding author.

allowed the Fe₃O₄@Carbon-based electrode to maintain its structural integrity during repeated Li⁺ insertion/extraction. Additionally, carbon coating on Fe₃O₄ provided a stable SEI film. The Fe₃O₄@Carbon composites exhibited high mechanical stability and excellent cycling performance (954 mAh·g⁻¹ 200 cycles at 0.5 A·g⁻¹) [21]. Liu *et al.* prepared micron-sized porous Fe₃O₄ spheres through the solvothermal and calcination methods. Carbon-covered Fe₃O₄ porous microspheres demonstrated an outstanding reversible capacity (747 mAh·g⁻¹ after 50 cycles at 0.1 A·g⁻¹) and good rate capacity (255 mAh·g⁻¹ at 1.6 A·g⁻¹) [22]. Zhou *et al.* synthesized uniform porous Fe₃O₄@Carbon microspheres by a hydrothermal method. These microspheres showed good electrochemical performance (609 mAh·g⁻¹ after 200 cycles at 0.2 A·g⁻¹) [23].

In this work, novel core-shell porous Fe₃O₄@C microspheres (CP-Fe₃O₄@C) were successfully designed and constructed by simple hydrothermal and carbonization methods. First, the Fe₃O₄@GU microspheres were synthesized using ferric chloride as an iron source and common chemicals glucose and urea as filler particles; the Fe₃O₄@GU composite was heat-treated in oxygen atmosphere to obtain the porous Fe₂O₃ microspheres. Second, resorcinol-formaldehyde (RF) resin was applied to porous Fe₂O₃ microspheres to obtain core-shell Fe₂O₃@RF microspheres, which were then used for the fabrication of CP-Fe₃O₄@C microspheres by one-step carbonization without a surfactant. The material synthesized through our straightforward method shows excellent performance as an anode material for LIBs.

2. Experimental section

2.1. Preparation of Fe₃O₄@GU

The Fe₃O₄@GU microspheres were prepared by a simple hydrothermal technique. Briefly, 2.13 g of ferric chloride (FeCl₃), 2.0 g of glucose (C₆H₁₂O₆) and 2.1 g of urea (CH₄N₂O) were added to 90 mL of deionized (DI) water and stirred. The resulting orange solution was placed into a 200 mL stainless steel Teflon-lined autoclave, heated at 200 °C for 6 h and then cooled to ambient temperature. The black Fe₃O₄@GU microspheres were washed with DI water thrice and dried at 60 °C for 12 h.

2.2. Preparation of porous Fe₂O₃

The Fe₃O₄@GU microspheres were heated at 500 °C in oxygen for 4 h, after which the furnace was cooled to the ambient temperature naturally. The bright orange porous Fe₂O₃ microspheres were washed with DI water thrice and dried at 60 °C for 12 h.

2.3. Preparation of CP-Fe₃O₄@C microspheres

A mixture containing 15 mL of DI water and 15 mL of ethanol was used to disperse porous Fe₂O₃ microspheres. Then, 2 mL of formaldehyde and 0.8 g of resorcinol were added, and the whole mixture was stirred for 30 min. The mixture was then transferred into a 100 mL stainless steel Teflon-lined autoclave and heated at 100 °C for 36 h. The resulting material (which was Fe₂O₃@RF composite) was calcined at 500 °C for 4 h under N₂ at a heating rate of 2 °C·min⁻¹ to produce CP-Fe₃O₄@C microspheres. A schematic of the the preparation process for CP-Fe₃O₄@C microspheres is shown in Figure 1.

2.4. Material characterization

Crystalline phases were confirmed by X-ray diffraction (XRD) using Cu K_α radiation (λ = 0.15406 nm) by a D8 type advanced diffractometer (40 kV and 30 mA). X-ray photoelectron spectroscopy (XPS) was performed at 280 eV using ESCALAB 250Xi operated using Al K_α radiation as an excitation source. Morphology and microstructure were characterized by field emission scanning electron microscopy (FE-SEM, Merlin Compact) and transmission electron microscopy (TEM, G2F20). Raman spectra were recorded using the Bruker-Senterra spectrometer with 514 nm laser excitation. Sample weight losses were measured by thermo-gravimetric analysis (TGA, HCT-3). The analysis was performed in air in a range of 30 to 800 °C at a heating rate of 10 °C·min⁻¹. The surface area of the CP-Fe₃O₄@C composite was measured by the Brunauer-Emmett-Teller (BET) method (Autosorb-IQ). Pore sizes were obtained from the corresponding nitrogen adsorption/desorption isotherms using the Barrett-Joyner-Halenda formula.

2.5. Electrochemical measurements

Anodes were prepared by mixing the active materials with conductive acetylene black and poly-vinylidene

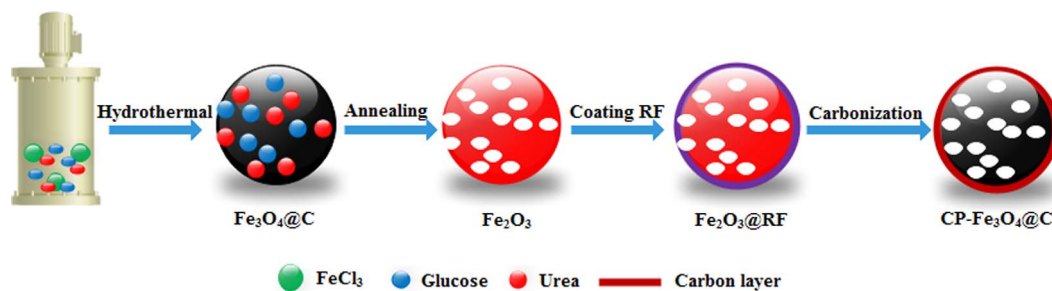


Figure 1. Synthesis flow chart of the CP-Fe₃O₄@C composite.

fluoride (PVDF) binder at a ratio of 8:1:1. The N-methyl pyrrolidone solvent (1.0 mL) was added to prepare slurry, which was applied to a copper foil and dried at 80 °C for 12 h. Coin cells (with standard size 2032) were assembled in a glove box under Ar atmosphere. Metallic Li was used as the counter electrode. The LiPF₆ (1.0 M) dissolved in a 1:1 ethylene carbonate:dimethyl carbonate mixture was used as the electrolyte. Galvanostatic charge–discharge (GCD) measurements at various current densities were recorded using NEWARE CT-4008 (Shenzhen). Cyclic voltammetry (CV) was measured using an electrochemical workstation (Solartron 1287) from a potential of 0.01 to 3.00 V at a 0.1 mV·s⁻¹ sweep rate. Electrochemical impedance spectroscopy was conducted on the electrochemical workstation (Solartron 1287) from 0.01 Hz to 100 kHz at a perturbation of 5 mVAC.

3. Results and discussion

As-prepared Fe₃O₄@GU, Fe₂O₃ and CP-Fe₃O₄@C microspheres were characterized by XRD (Figure 2a). The strong reflections of Fe₂O₃ microspheres observed at 2 θ = 24.2, 33.2, 35.7, 40.9, 49.5, 54.0, 62.4 and 64.0° correspond to the (012), (104), (110), (113), (024), (116), (214) and (330) planes of hematite (JCPDS 33-0664) [24]. The XRD of Fe₃O₄@GU and CP-Fe₃O₄@C microspheres showed several peaks that are consistent with the face-centered Fe₃O₄ phase (JCPDS 19-0624) [12,25]. In addition, no peaks of Fe₂O₃ were found in the diffraction peak of CP-Fe₃O₄@C, indicating that Fe₂O₃ was converted to Fe₃O₄. The carbon content analyses for Fe₃O₄@GU, Fe₂O₃ and CP-Fe₃O₄@C materials are shown in Figure 2b. Fe₂O₃ demonstrated almost no carbon

weight loss and was corroborated by the XRD showing that only a Fe₂O₃ phase was present in this sample. There was rapid weight loss for Fe₃O₄@GU and CP-Fe₃O₄@C occurring from 200 to 400 °C, which was attributed to the decomposition of the carbon layer. With this weight loss, it was determined that the carbon content values for the Fe₃O₄@GU and CP-Fe₃O₄@C microspheres were 37.61% and 17.35%, respectively.

Raman spectra showed the presence of carbon in the CP-Fe₃O₄@C microspheres (see Supplementary Figure S1), indicated by the presence of two broad peaks at 1349 and 1587 cm⁻¹, which correspond to D and G bands. These bands are assigned to sp³ disordered and sp² ordered graphitic carbon bonds [26]. The ratio between D and G bands (I_D/I_G) is often used to evaluate the degree of carbon graphitization. For the CP-Fe₃O₄@C microspheres, the ratio was 0.96, and this suggests a high degree of graphitization in the carbon coating of the Fe₃O₄ microspheres. This graphitization is beneficial for electrical conductivity of the composite [27].

The nitrogen absorption/desorption isotherms of CP-Fe₃O₄@C show a hysteresis from 0.5 to 1.0 relative pressure (see Figure 2c). The BET surface area of the CP-Fe₃O₄@C was equal to 16.8 m²·g⁻¹. The pore size distribution curve shows a peak near 3.8 nm (see insert in Figure 2c), evincing a nanopore presence. High surface area and porosity provide good contact between the electrode material and the electrolyte. This in turn promotes Li⁺ diffusion and allows active material to adapt to the volume expansion [28].

The XPS of CP-Fe₃O₄@C microspheres shows peaks corresponding to Fe, C and O (see Figure 2d). High-resolution scans and curve fitting show Fe peaks at 711.2 and 724.8 eV, which belong to Fe 2p_{3/2}

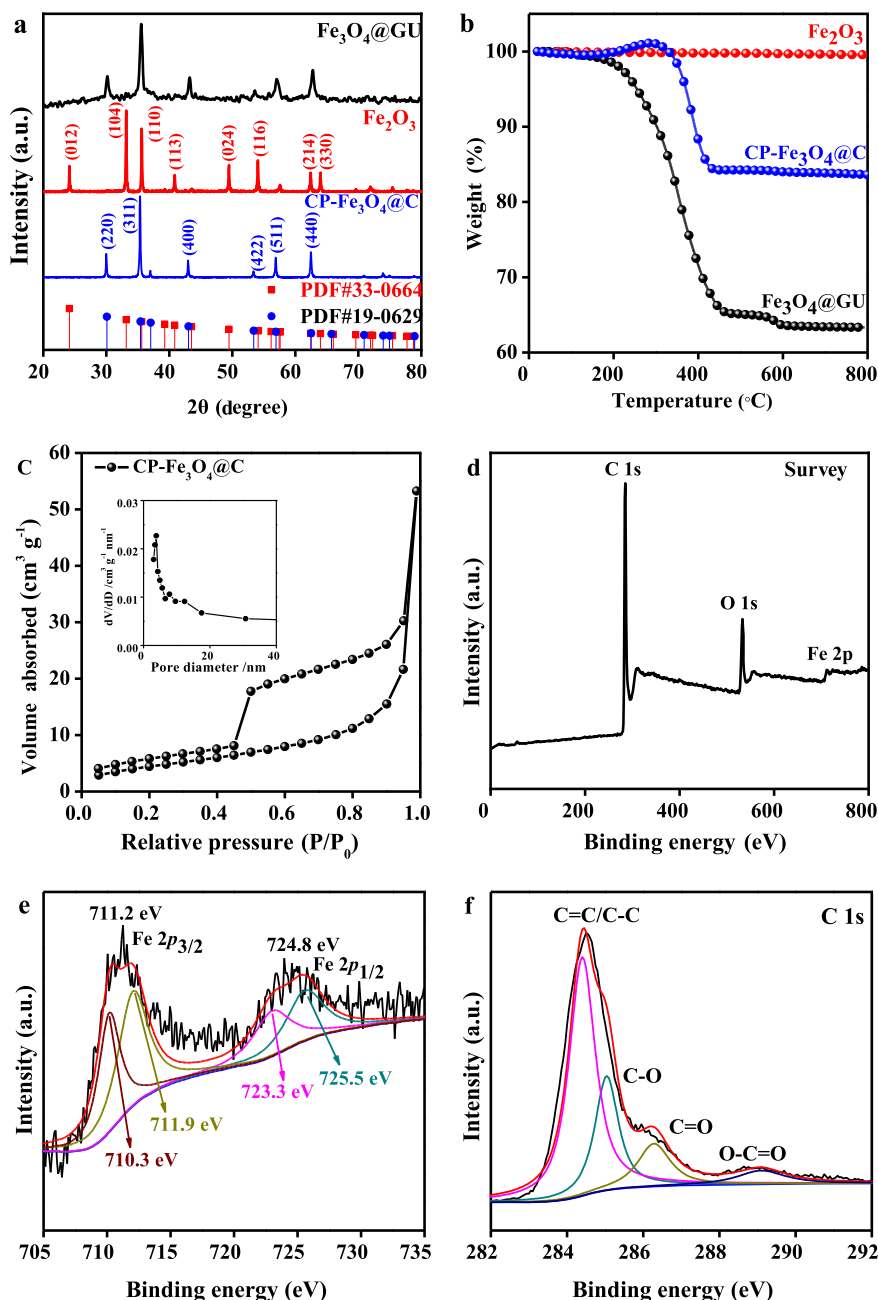


Figure 2. Sample characterization. (a) XRD pattern, (b) TGA pattern, (c) nitrogen adsorption/desorption isotherms and pore size distribution curve (inset), XPS spectra of the $\text{CP-Fe}_3\text{O}_4@C$ (d) survey, (e) Fe 2p , (f) C 1s .

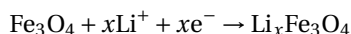
and $\text{Fe 2p}_{1/2}$, respectively (see Figure 2e), which are typical of Fe_3O_4 -based materials [29,30]. Two pairs of peaks at 710.3 and 723.3 eV and at 711.9 and 725.5 eV correspond to $\text{Fe 2p}_{3/2}$ and $\text{Fe 2p}_{1/2}$

of Fe^{2+} and Fe^{3+} , respectively [31]. High-resolution scans of C 1s (see Figure 2f) show peaks at 284.4 (typical of sp^2 -hybridized graphitic C), 285.0 eV (attributed to the sp^3 -hybridized C) and at 286.3 and

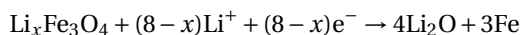
289.0 eV (both of which are attributed to the carbon layer surface functional groups such as C=O and O=C=O) [32].

The SEM of Fe₃O₄@GU microspheres demonstrated particles with uniform spherical shapes with an average diameter of 250 nm (see Figure 3a). After annealing, Fe₃O₄@GU microspheres were completely converted to Fe₂O₃ microspheres (Figure 3b) as supported by XRD. The surface of the Fe₂O₃ microspheres shows strong porosity unlike Fe₃O₄@GU microspheres. Micrographs of the CP-Fe₃O₄@C microspheres obtained after carbon coating of Fe₂O₃ microspheres are shown in Figure 3c. It can be seen that the surfaces of the CP-Fe₃O₄@C microspheres are smooth compared to those of the Fe₂O₃ microspheres because the carbon layer was successfully coated. Figures 3d, e and f are TEM images of Fe₃O₄@GU, Fe₂O₃ and CP-Fe₃O₄@C microspheres, respectively. From these three figures, it can be seen that both Fe₂O₃ and CP-Fe₃O₄@C microspheres show clear porosity, while Fe₃O₄@GU microspheres exhibit almost none. The TEM image of the CP-Fe₃O₄@C microspheres shows a thin carbon outer layer approximately 20 nm thick (see Supplementary Figure S2). High-resolution TEM images of the CP-Fe₃O₄@C microspheres (Supplementary Figure S3) show distinct lattice fringes with a spacing of 0.252 nm, which corresponds to the (311) planes of cubic Fe₃O₄. The scanning TEM image of the CP-Fe₃O₄@C microspheres (Figure 3g) and the corresponding element mapping (Figure 3h–j) further establish that CP-Fe₃O₄@C microspheres were successfully carbon-coated.

Cyclic voltammetry of the CP-Fe₃O₄@C electrode displays a definite reduction peak at 0.2–0.8 V during the first discharge (Figure 4a), which corresponds to the structural transformation caused by lithium incorporation according to the chemical reaction:



Further conversion of Li_xFe₃O₄ to Fe(0) occurs according to the reaction [5,33]:



During subsequent cycles, lithium insertion at the cathode occurred mainly between 0.58 and 1.15 V, and lithium extraction at the anode mainly occurred between 1.38 and 2.11 V. It is worth noting that

the 2nd, 3rd, and 10th cycles of CV almost coincide, indicating that the electrode cycling process has a minimal impact on subsequent cycles. Figure 4b shows the GCD of the CP-Fe₃O₄@C electrode after the 1st, 2nd, 3rd, 50th, 100th and 200th cycles at 0.3 A·g⁻¹ between 0.01 and 3.0 V. The initial discharge curve showed a plateau between 0.21 and 0.66 V. The second and subsequent discharge voltages increased to 0.62–1.10 V, which is consistent with CV. The initial discharge and charge capacity of the CP-Fe₃O₄@C electrode were 1291 and 914 mAh·g⁻¹. These drastic differences in capacity usually stem from the formation of the SEI and often occur during the first cycle. The stability and capacity of the CP-Fe₃O₄@C electrode were compared to those of the Fe₃O₄@GU and Fe₂O₃ electrodes (see Figure 4c). After 200 cycles at 0.3 A·g⁻¹, the reversible capacities of the CP-Fe₃O₄@C, Fe₃O₄@GU and Fe₂O₃ electrodes were 785, 508 and 203 mAh·g⁻¹, respectively. It is clear that the porous core-shell structure of the CP-Fe₃O₄@C electrode plays a critical role in the electrochemical performance. Experimentally obtained electrochemical characteristics of different Fe₃O₄@carbon electrodes with respect to their corresponding Li storage capacity are shown in Supplementary Table S1. The rate capability of the CP-Fe₃O₄@C electrode is shown in Figure 4d. The stable discharge capacities of the CP-Fe₃O₄@C electrode at 0.3, 0.8, 1.6, 3 and 6 A·g⁻¹ were ~791, 648, 471, 312, and 130 mAh·g⁻¹, respectively. Additionally, the discharge capacity value returned to 723 mAh·g⁻¹ after the current density was reduced back to 0.3 A·g⁻¹. These results demonstrate that the CP-Fe₃O₄@C electrode has outstanding rate capability, high reversibility, and stability for LIBs. Figure 4e shows the charge–discharge curves of the anodes containing CP-Fe₃O₄@C microspheres as the active material at various current densities. The charge–discharge voltage plateau gradually sloped as the current density was increased, but even at a current density of 6 A·g⁻¹, the charge–discharge voltage plateaus still persisted.

The electrochemical impedance behavior of the CP-Fe₃O₄@C electrode under different current cycles at the same current density was studied using Nyquist plots (see Figure 4f). All plots exhibit semi-circles in the high- and intermediate-frequency regions and oblique curves at low frequencies. Additionally, equivalent circuit modeling (top right insets,

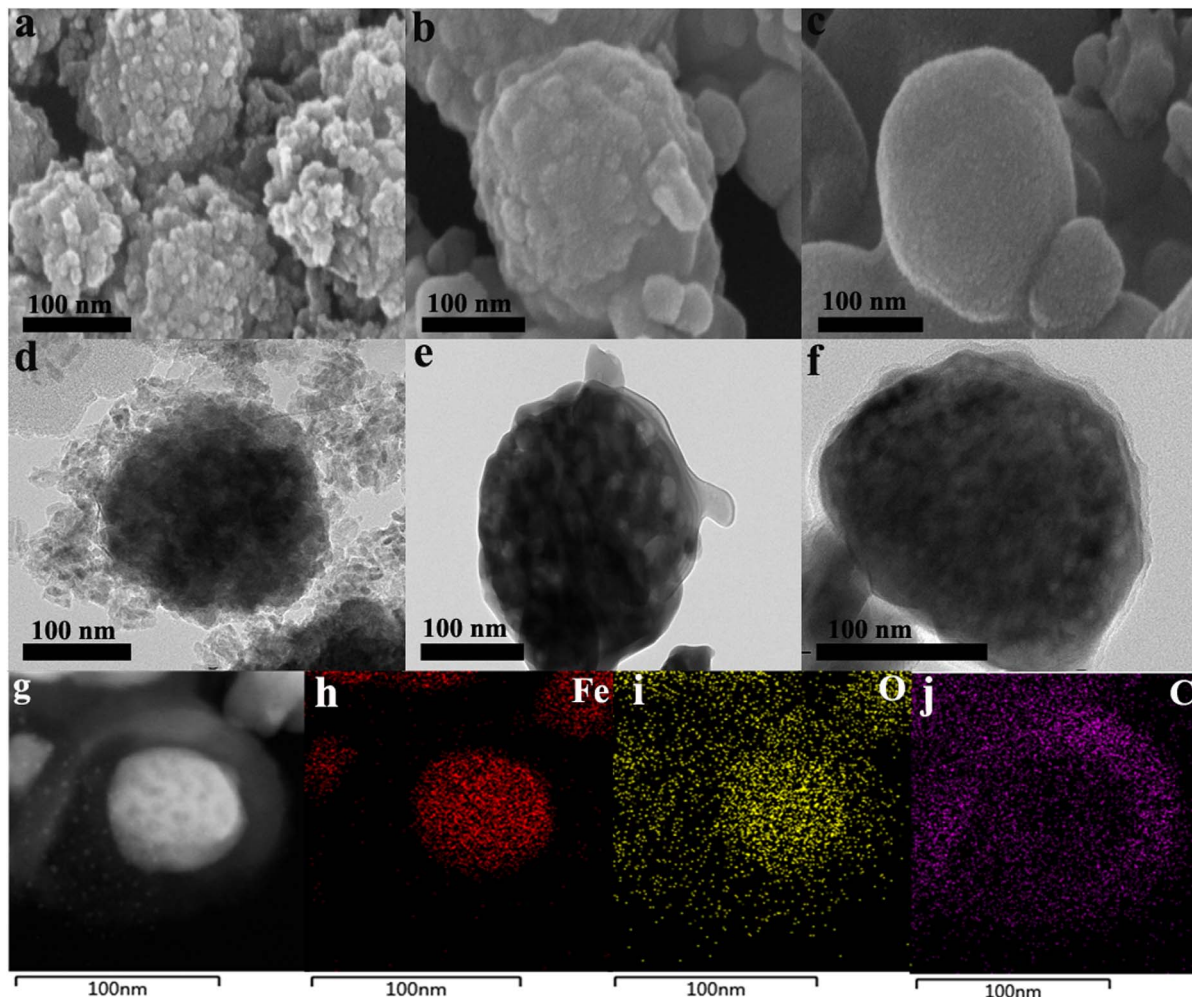


Figure 3. SEM images of (a) Fe₃O₄@GU, (b) Fe₂O₃ and (c) CP-Fe₃O₄@C composites. TEM images of (d) Fe₃O₄@GU, (e) Fe₂O₃ and (f) CP-Fe₃O₄@C composites. EDX elemental mapping of (g-j) CP-Fe₃O₄@C composite.

Figure 4f) was carried out using Z-VIEW software to obtain kinetic parameters of three composites. According to the equivalent circuit diagram, the intercept of the high-frequency semicircle with the x -axis corresponds to the electrolyte resistance (R_e), while R_f and R_{ct} correspond to SEI film and charge transfer resistances, respectively [27,34]. The slope at low frequencies corresponds to the Warburg impedance (Z_w) of the Li⁺ diffusion; CPE1 and CPE2 are the SEI film and double layer capacitances, respectively [35, 36]. CP-Fe₃O₄@C-based anodes exhibited lower R_{ct} values (which were equal to 16.5 Ω) after the first cycle, especially when compared to R_{ct} values of the

fresh cycle (which was equal to 395.7 Ω). This difference is mainly due to the wetting of the electrode and proper SEI formation during the first cycle. The R_{ct} value after the 200th cycle differs only slightly from the R_{ct} value after the 100th cycle, again pointing to an excellent electrode structural stability. Resistance values of electrodes based on Fe₃O₄@GU and Fe₂O₃ active materials were higher than the total resistance of the CP-Fe₃O₄@C-based electrodes for all cycles tested in this work (see Supplementary Figures S4a and S4b).

The rate performance of CP-Fe₃O₄@C-based LIB anodes as well as their reaction kinetics was analyzed

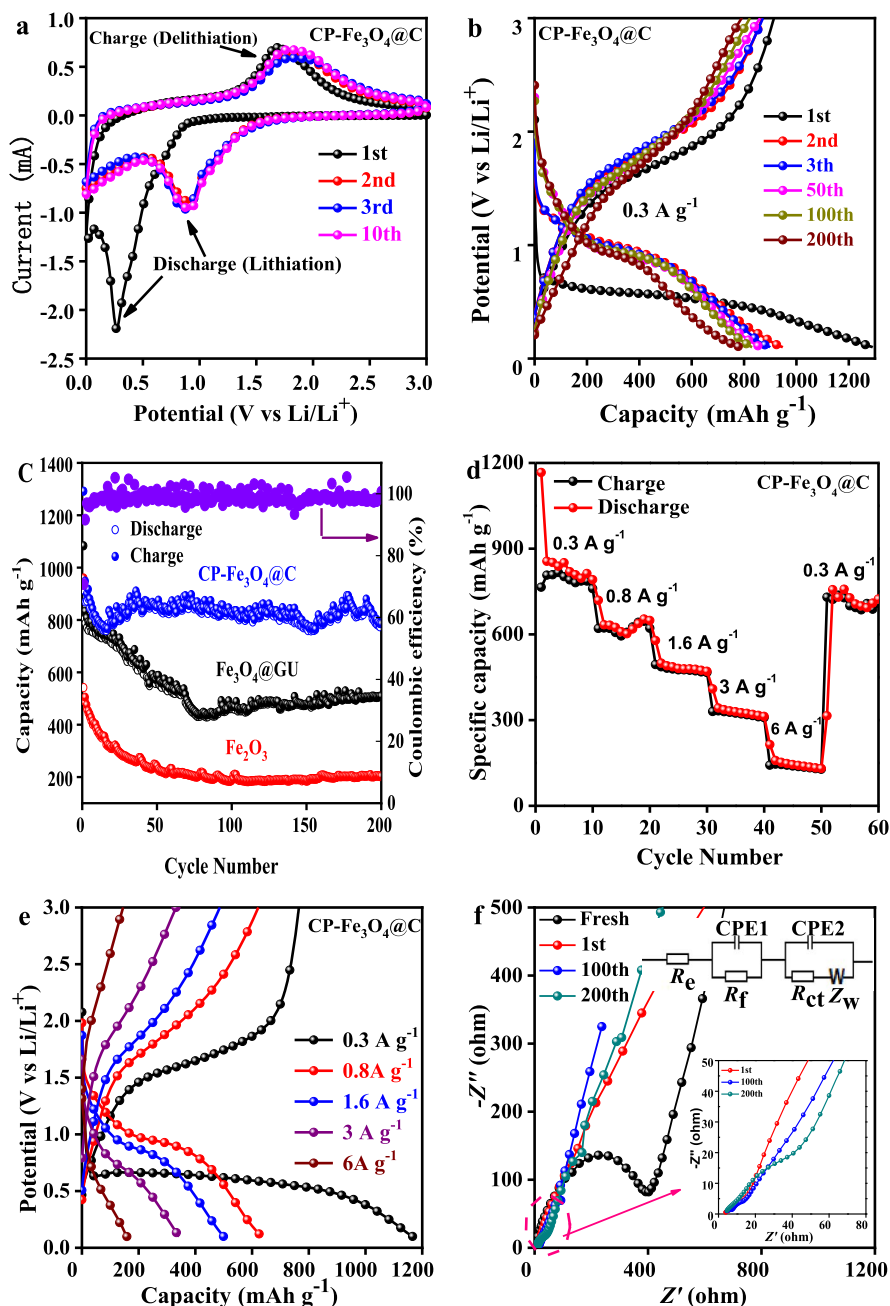


Figure 4. (a) CV curves at $0.1 \text{ mV}\cdot\text{s}^{-1}$ and (b) GCD curves at $0.3 \text{ A}\cdot\text{g}^{-1}$ of the CP-Fe₃O₄@C electrode. (c) Cyclic performance at $0.3 \text{ A}\cdot\text{g}^{-1}$ of the Fe₂O₃, Fe₃O₄@GU and CP-Fe₃O₄@C electrodes. (d) Rate performance at different current densities. (e) Representative discharge–charge voltage profiles at various rates. (f) Nyquist plots of the CP-Fe₃O₄@C electrode (top right insets show the equivalent circuit model).

by CV. The contribution of capacitance is calculated and identified using gradually increasing sweep rates

during CV as shown in Figure 5a. Using the method of Dunn [37,38], the total current response (i) at con-

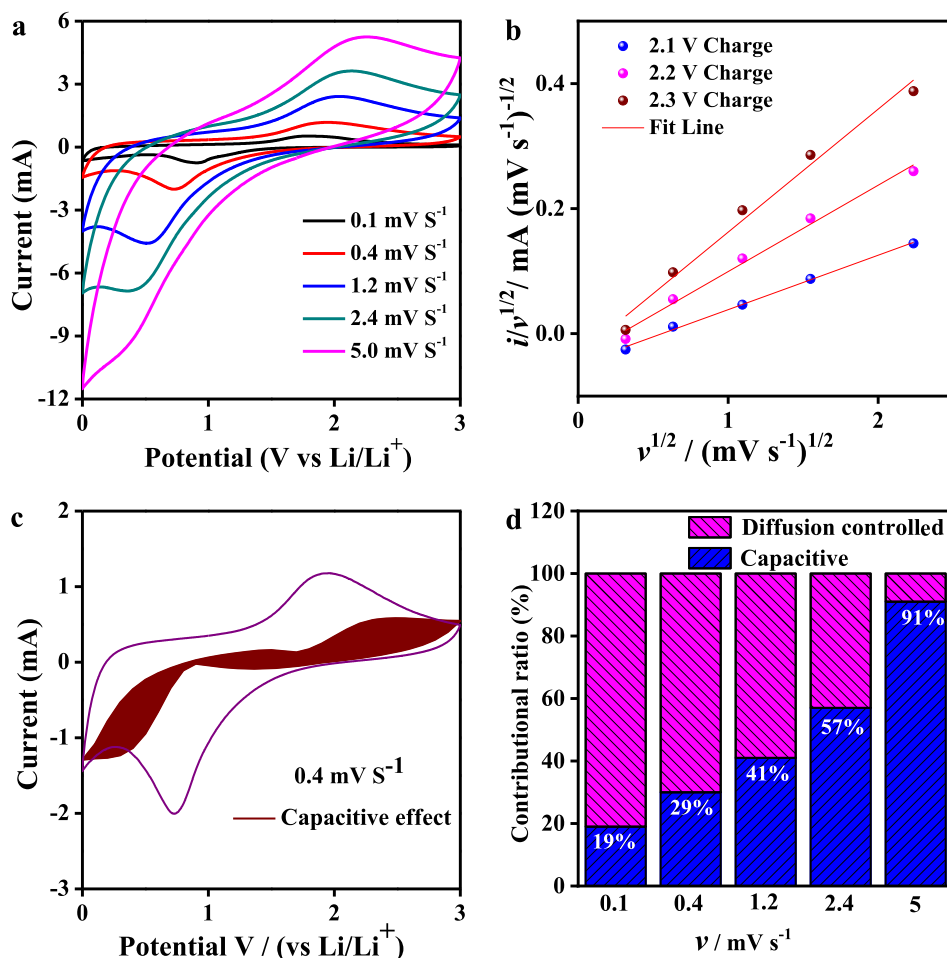


Figure 5. (a) CV curves at different scan rates from 0.1 to 5 mV·s⁻¹. (b) The fitted lines of $i(V)/v^{1/2}$ versus $i/v^{1/2}$ at different voltages. (c) CV curves with capacitive contribution at 0.4 mV·s⁻¹. (d) Separation of contributions from capacitive effects and diffusion-controlled capacities at different scan rates.

stant potential (V) can be represented as a combination of surface capacitive effects and diffusion-controlled insertion processes (see (1) and (2)):

$$i(V) = K_1 v + K_2 v^{1/2}, \quad (1)$$

$$i(V)/v^{1/2} = K_1 v^{1/2} + K_2, \quad (2)$$

where $K_1 v$ and $K_2 v^{1/2}$ are the contributions of the total surface capacitive and diffusion-controlled insertion processes, respectively. Comparing CV results at different sweeps, the values of K_1 and K_2 can be determined by fitting $i(V)/v^{1/2}$ versus $v^{1/2}$ as a linear function according to (2) as shown in Figure 5b. Subsequently, K_1 and K_2 are replaced by their values in (1), partitioning the contribution of Faradic ca-

capacity from the contribution of pseudocapacitance in the total stored charge. Figure 5c shows a separation of capacitance and diffusion currents at a scan rate of 0.4 mV·s⁻¹. Brown areas represent capacitance effect, and blank areas represent diffusion-controlled capabilities. As can be seen from Figure 5d, at 0.1, 0.4, 1.2, 2.4 and 5 mV·s⁻¹, pseudocapacitance accounts for 19%, 29%, 41%, 57% and 91%, respectively, of the total capacity, indicating significant pseudocapacitance behavior during the cycling of CP-Fe₃O₄@C-based anodes at high rates. Thus, CP-Fe₃O₄@C-based electrodes demonstrated higher pseudocapacitance contribution at almost all current densities, which is indicative of an excellent rate performance.

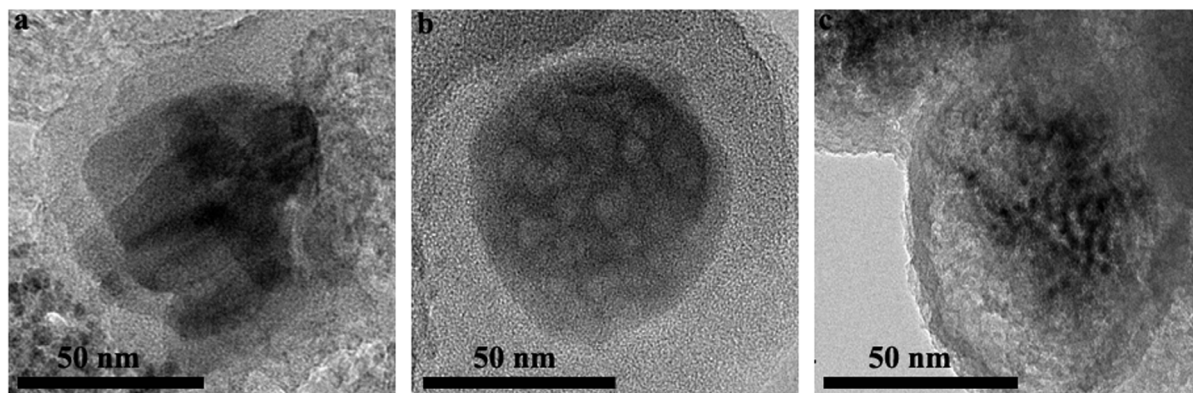


Figure 6. CP-Fe₃O₄@C electrode: (a) before cycle, (b) after 10 cycles and (c) after 60 cycles.

The morphology of the CP-Fe₃O₄@C-based electrode was tested before cycling and also after 10 and 60 cycles (Figure 6). Fe₃O₄ microspheres in prepared CP-Fe₃O₄@C electrode material are uniformly wrapped by a carbon layer (see Figure 6a). The carbon coating on the CP-Fe₃O₄@C electrode after the 10th cycle is still intact, and the carbon layer is mostly unchanged (see Figure 6b). After the 60th cycle, Fe₃O₄ structurally deteriorates into smaller microspheres, but Fe₃O₄ remains well coated with carbon layers (see Figure 6c).

4. Conclusions

In summary, the core-shell CP-Fe₃O₄@C microspheres were synthesized by simple methods using common inexpensive and easily removable chemicals as filler particles. The unique structural characteristics of the CP-Fe₃O₄@C microspheres yielded electrodes with capacities equal to 785 mAh·g⁻¹ (at 0.3 A·g⁻¹ after 200 cycles). In addition, it was further shown that the CP-Fe₃O₄@C electrode has excellent rate performance through reaction kinetics. These experimental results show that the CP-Fe₃O₄@C composite prepared by this simple method has strong prospects as an active anode material for high-performance LIBs.

Conflicts of interest

The authors declare no conflict of interest.

Acknowledgment

This research was supported by the Future Scientists Program of “Double First Class” of China University of Mining and Technology (No. 2019WLKXJ025).

Supplementary data

Supporting information for this article is available on the journal’s website under <https://doi.org/10.5802/crchim.18> or from the author.

References

- [1] M. Armand, J. M. Tarascon, “Building better batteries”, *Nature*, 2008, **451**, 652-657.
- [2] M. Reddy, G. Rao, B. Chowdari, “Metal oxides and oxysalts as anode materials for Li ion batteries”, *Chem. Rev.*, 2013, **113**, 5364-5457.
- [3] Y. Fu, Y. He, L. Qu, Y. Feng, J. Li, J. Liu, G. Zhang, W. Xie, “Enhancement in leaching process of lithium and cobalt from spent lithium-ion batteries using benzenesulfonic acid system”, *Waste Manage.*, 2019, **88**, 191-199.
- [4] P. Poizot, S. Laruelle, S. Grugeon, L. Dupont, J. Tarascon, “Nano-sized transition-metal oxides as negative-electrode materials for lithium-ion batteries”, *Nature*, 2000, **407**, 496-499.
- [5] Y. Huang, Z. Xu, J. Mai, T.-K. Lau, X. Lu, Y.-J. Hsu, Y. Chen, A. C. Lee, Y. Hou, Y. S. Meng, Q. Li, “Revisiting the origin of cycling enhanced capacity of Fe₃O₄ based nanostructured electrode for lithium ion batteries”, *Nano Energy*, 2017, **41**, 426-433.
- [6] Q. Wu, R. Jiang, L. Mu, S. Xu, “Fe₃O₄ anodes for lithium batteries: production techniques and general applications”, *C. R. Chim.*, 2019, **22**, 96-102.
- [7] P. L. Taberna, S. Mitra, P. Poizot, P. Simon, J. M. Tarascon, “High rate capabilities Fe₃O₄-based Cu nano-architected electrodes for lithium-ion battery applications”, *Nat. Mater.*, 2006, **5**, 567-573.

- [8] S. Yuan, X. Bo, L. Guo, "In-situ insertion of multi-walled carbon nanotubes in the Fe₃O₄/N/C composite derived from iron-based metal-organic frameworks as a catalyst for effective sensing acetaminophen and metronidazole", *Talanta*, 2019, **193**, 100-109.
- [9] H. L. Karlsson, P. Cronholm, J. Gustafsson, L. Möller, "Copper oxide nanoparticles are highly toxic: a comparison between metal oxide nanoparticles and carbon nanotubes", *Chem. Res. Toxicol.*, 2008, **21**, 1726-1732.
- [10] E. Kang, Y. S. Jung, A. S. Cavanagh, G.-H. Kim, S. M. George, A. C. Dillon, J. K. Kim, J. Lee, "Fe₃O₄ nanoparticles confined in mesocellular carbon foam for high performance anode materials for lithium-ion batteries", *Adv. Funct. Mater.*, 2011, **21**, 2430-2438.
- [11] T. Yoon, C. Chae, Y.-K. Sun, X. Zhao, H. H. Kung, J. K. Lee, "Bottom-up in situ formation of Fe₃O₄ nanocrystals in a porous carbon foam for lithium-ion battery anodes", *J. Mater. Chem.*, 2011, **21**, 17325-17330.
- [12] G. Zhou, D.-W. Wang, F. Li, L. Zhang, N. Li, Z. S. Wu, L. Wen, G. Q. Lu, H.-M. Cheng, "Graphene-wrapped Fe₃O₄ anode material with improved reversible capacity and cyclic stability for lithium ion batteries", *Chem. Mater.*, 2010, **22**, 5306-5313.
- [13] J. Su, M. Cao, L. Ren, C. Hu, "Fe₃O₄-graphene nanocomposites with improved lithium storage and magnetism properties", *J. Phys. Chem. C*, 2011, **115**, 14469-14477.
- [14] E. Yoo, J. Kim, E. Hosono, H.-S. Zhou, T. Kudo, I. Honma, "Large reversible Li storage of graphene nanosheet families for use in rechargeable lithium ion batteries", *Nano Lett.*, 2008, **8**, 2277-2282.
- [15] D. Golberg, Y. Bando, Y. Huang, T. Terao, M. Mitome, C. Tang, C. Zhi, "Boron nitride nanotubes and nanosheets", *ACS Nano*, 2010, **4**, 2979-2993.
- [16] J. Luo, J. Liu, Z. Zeng, C. F. Ng, L. Ma, H. Zhang, J. Lin, Z. Shen, H. J. Fan, "Three-dimensional graphene foam supported Fe₃O₄ lithium battery anodes with long cycle life and high rate capability", *Nano Lett.*, 2013, **13**, 6136-6143.
- [17] X. Lu, R. Wang, Y. Bai, J. Chen, J. Sun, "Facile preparation of a three-dimensional Fe₃O₄/macroporous graphene composite for high-performance Li storage", *J. Mater. Chem. A*, 2015, **3**, 12031-12037.
- [18] P. Salimi, O. Norouzi, S. E. M. Pourhosseini, "Two-step synthesis of nanohusk Fe₃O₄ embedded in 3D network pyrolytic marine biochar for a new generation of anode materials for lithium-ion batteries", *J. Alloys Compd.*, 2019, **786**, 930-937.
- [19] S. E. M. Pourhosseini, O. Norouzi, P. Salimi, H. R. Naderi, "Synthesis of a novel interconnected 3D pore network algal biochar constituting iron nanoparticles derived from a harmful marine biomass as high-performance asymmetric supercapacitor electrodes", *ACS Sustain. Chem. Eng.*, 2018, **6**, 4746-4758.
- [20] H. Yu, G. Guo, L. Ji, H. Li, D. Yang, J. Hu, A. Dong, "Designed synthesis of ordered mesoporous graphene spheres from colloidal nanocrystals and their application as a platform for high-performance lithium-ion battery composite electrodes", *Nano Res.*, 2016, **9**, 3757-3771.
- [21] B. Wang, X. Zhang, X. Liu, G. Wang, H. Wang, J. Bai, "Rational design of Fe₃O₄@C yolk-shell nanorods constituting a stable anode for high-performance Li/Na-ion batteries", *J. Colloid Interface Sci.*, 2018, **528**, 225-236.
- [22] R. Liu, T. Li, F. Han, Y. Bai, Y. Qi, N. Lun, "Thermal formation of porous Fe₃O₄/C microspheres and the lithium storage performance", *J. Alloys Compd.*, 2014, **597**, 30-35.
- [23] Z. Zhou, W. Xie, S. Li, X. Jiang, D. He, S. Peng, F. Ma, "Facile synthesis of porous Fe₃O₄@C nanospheres as high-performance anode for lithium-ion battery", *J. Solid State Electr.*, 2015, **19**, 1211-1215.
- [24] J. Zhu, K. Y. S. Ng, D. Deng, "Porous olive-like carbon decorated Fe₃O₄ based additive-free electrodes for highly reversible lithium storage", *J. Mater. Chem. A*, 2014, **2**, 16008-160014.
- [25] Y. Wang, Y. Gao, J. Shao, R. Holze, Z. Chen, Y. Yun, Q. Qu, H. Zheng, "Ultrasmall Fe₃O₄ nanodots within N-doped carbon frameworks from MOFs uniformly anchored on carbon nanowebbs for boosting Li-ion storage", *J. Mater. Chem.*, 2018, **6**, 3659-3666.
- [26] K. N. Kudin, B. Ozbas, H. C. Schniepp, R. K. Prudhomme, I. A. Aksay, R. Car, "Raman spectra of graphite oxide and functionalized graphene sheets", *Nano Lett.*, 2008, **8**, 36-41.
- [27] L. Ma, R. Chen, G. Zhu, Y. Hu, Y. Wang, T. Chen, J. Liu, Z. Jin, "Cerium oxide nanocrystal embedded bimodal micromesoporous nitrogen-rich carbon nanospheres as effective sulfur host for lithium-sulfur batteries", *ACS Nano*, 2017, **11**, 7274-7183.
- [28] Q. Xiong, Y. Lu, X. Wang, C. Gu, Y. Qiao, J. Tu, "Improved electrochemical performance of porous Fe₃O₄/carbon core/shell nanorods as an anode for lithium-ion batteries", *J. Alloys Compd.*, 2012, **536**, 219-225.
- [29] T. Fujii, F. M. F. de Groot, G. A. Sawatzky, F. C. Voigt, T. Hibma, K. Okada, "In situ XPS analysis of various iron oxide films grown by NO₂-assisted molecular-beam epitaxy", *Phys. Rev. B*, 1999, **59**, 3195-3202.
- [30] C. Liao, S. Wu, "Pseudocapacitance behavior on Fe₃O₄-pillared SiO_x micro-sphere wrapped by graphene as high performance anodes for lithium-ion batteries", *Chem. Eng. J.*, 2019, **355**, 805-814.
- [31] B. Liu, Q. Zhang, Z. Jin, L. Zhang, L. Li, Z. Gao, C. Wang, H. Xie, Z. Su, "Uniform pomegranate-like nanoclusters organized by ultrafine transition metal oxide@nitrogen-doped carbon subunits with enhanced lithium storage properties", *Adv. Eng. Mater.*, 2017, **8**, 1702347-1702355.
- [32] X. Wang, K. Chen, G. Wang, X. Liu, H. Wang, "Rational design of three-dimensional graphene encapsulated with hollow FeP@carbon nanocomposite as outstanding anode material for lithium ion and sodium ion batteries", *ACS Nano*, 2017, **11**, 11602-11616.
- [33] L. Li, A. Kovalchuk, H. Fei, Z. Peng, Y. Li, N. D. Kim, C. Xi, Y. Yang, G. Ruan, J. M. Tour, "Enhanced cycling stability of lithium-ion batteries using graphene-wrapped Fe₃O₄-graphene nanoribbons as anode materials", *Adv. Eng. Mater.*, 2015, **5**, 1500171-1500176.
- [34] Y. Wang, Y. Jin, C. Zhao, E. Pan, M. Jia, "Fe₃O₄ nanoparticle/graphene aerogel composite with enhanced lithium storage performance", *Appl. Surf. Sci.*, 2018, **458**, 1035-1042.
- [35] S. Zhang, L. Zhu, H. Song, X. Chen, J. Zhou, "Enhanced electrochemical performance of MnO nanowire/graphene composite during cycling as the anode material for lithium-ion batteries", *Nano Energy*, 2014, **10**, 172-180.

- [36] K. Zhang, P. Han, L. Gu, L. Zhang, Z. Liu, Q. Kong, C. Zhang, S. Dong, Z. Zhang, J. Yao, H. Xu, G. Cui, L. Chen, "Synthesis of nitrogen-doped MnO/graphene nanosheets hybrid material for lithium ion batteries", *ACS Appl. Mater. Interface*, 2012, **4**, 658-664.
- [37] J. Wang, J. Polleux, J. Lim, B. Dunn, "Pseudocapacitive contributions to electrochemical energy storage in TiO₂ (anatase) nanoparticles", *J. Phys. Chem. C*, 2017, **111**, 14925-14931.
- [38] L. C. Liu, W. G. Pell, B. E. Conway, "Behavior of molybdenum nitrides as materials for electrochemical capacitors: comparison with ruthenium oxide", *J. Electrochem. Soc.*, 1998, **145**, 1882-1888.